nature neuroscience

Early hyperactivity and precocious maturation of corticostriatal circuits in *Shank3B*$^{-/-}$ mice

Rui T Peixoto, Wengang Wang, Donyell M Croney, Yevgenia Kozorovitskiy & Bernardo L Sabatini

Some autistic individuals exhibit abnormal development of the caudate nucleus and associative cortical areas, suggesting potential dysfunction of cortico-basal ganglia (BG) circuits. Using optogenetic and electrophysiological approaches in mice, we identified a narrow postnatal period that is characterized by extensive glutamatergic synaptogenesis in striatal spiny projection neurons (SPNs) and a concomitant increase in corticostriatal circuit activity. SPNs during early development have high intrinsic excitability and respond strongly to cortical afferents despite sparse excitatory inputs. As a result, striatum and corticostriatal connectivity are highly sensitive to acute and chronic changes in cortical activity, suggesting that early imbalances in cortical function alter BG development. Indeed, a mouse model of autism with deletions in *Shank3* (*Shank3B*$^{-/-}$) shows early cortical hyperactivity, which triggers increased SPN excitatory synapse and corticostriatal hyperconnectivity. These results indicate that there is a tight functional coupling between cortex and striatum during early postnatal development and suggest a potential common circuit dysfunction that is caused by cortical hyperactivity.

The BG are a group of phylogenetically conserved subcortical nuclei involved in the generation of purposeful movements and experience-dependent acquisition of complex motor skills and behavioral strategies[1]. The striatum is the largest nucleus of the BG and receives diverse inputs from multiple brain regions, including glutamatergic projections from cortex that convey sensorimotor as well as cognitive information. Corticostriatal afferents synapse onto SPNs, which project to output BG nuclei that modulate cortex and several motor centers, forming a series of recurrent circuit loops[1,2]. Despite the central role of BG in controlling human behavior and their implication in numerous neurodevelopmental disorders, little is known about the early development of corticostriatal circuits. Studies across species have shown protracted maturation of SPN morphology and function for several weeks to months after birth[3–5]. However, perturbing striatal activity during early postnatal periods in mice alters corticostriatal connectivity as early as postnatal day 14 (P14), indicating that cortico-BG circuits are functional early in development and that recurrent network activity regulates BG circuit maturation[6].

A subset of autistic individuals exhibit dysmorphic striatal regions, suggesting that BG circuit dysfunction may contribute to the pathophysiology of autism spectrum disorders (ASDs)[7–10]. In addition, autism-associated behaviors, such as limited and obsessive interests and motor stereotypies, are hallmarks of other BG-associated disorders, such as Tourette's and obsessive compulsive disorders (OCDs)[1,11,12]. Increasing evidence suggests a strong genetic component in the etiology of ASDs, with many associated genes encoding proteins involved in glutamatergic synapse development and function[13,14]. In particular, *SHANK3* is highly prevalent in ASDs, with full deletions found in a large fraction of Phelan-McDermid syndrome cases and rare mutations associated with idiopathic ASDs[14–16]. Shank family proteins are postsynaptic scaffolds at glutamatergic synapses, where they organize an extensive protein complex[14]. Overexpression of Shank3 in dissociated neuronal cultures increases synapse formation and strength[17,18], whereas transgenic overexpression *in vivo* increases dendritic spines in hippocampus[19]. Conversely, knockdown of Shank3 reduces spine density in dissociated hippocampal neurons, suggesting a correlation between Shank3 levels and excitatory synapse number[20]. Notably, Shank3 is the only Shank expressed in the mouse striatum, and mice with *Shank3* deletions exhibit repetitive behaviors and reduced social interactions, two behavioral hallmarks of ASDs[21–24]. In particular, deletion of exons encoding the PDZ domain of Shank3 (*Shank3B*$^{-/-}$) increases striatal volume and reduces corticostriatal transmission in adults[23]. Given the developmental trajectory of ASD symptoms and the implication of Shank3 in glutamatergic synapse maturation, the corticostriatal phenotype exhibited by adult *Shank3B*$^{-/-}$ mice could have a developmental origin.

We examined the development of corticostriatal circuits in mice by combining optogenetic approaches with *in vitro* and *in vivo* electrophysiological analyses. We found that SPNs are primed to respond to cortical activity from very early developmental stages and undergo a phase of rapid maturation from P10–18. During this period, corticostriatal connectivity is highly sensitive to acute and chronic changes in cortical activity, suggesting that early imbalances in cortical function can impair BG circuit development. To our surprise, we found that *Shank3B*$^{-/-}$ mice exhibit precocious maturation of SPN excitatory inputs as a result of increased corticostriatal network activity. These results reveal a developmental circuit defect induced by the loss of Shank3 and suggest that abnormal corticostriatal maturation may be a common aspect of disorders with early imbalances in cortical activity.

Department of Neurobiology, Howard Hughes Medical Institute, Harvard Medical School, Boston, Massachusetts, USA. Correspondence should be addressed to B.L.S. (bsabatini@hms.harvard.edu).

Received 20 July 2015; accepted 29 January 2016; published online 29 February 2016; doi:10.1038/nn.4260

RESULTS

Rapid SPN excitatory synapse development after ~P10

To characterize the development of excitatory afferents onto SPNs, we measured optically evoked excitatory postsynaptic currents (oEPSCs) in dorsomedial striatum of P6–30 mice. Channelrhodopsin (ChR2) was expressed in a subset of corticostriatal projection neurons using *Rbp4-Cre;Ai32* (*Rbp4-Cre;ChR2$^{f/f}$*) transgenic mice[25]. These mice express Cre in layer 5 pyramidal neurons and activate ChR2(H134R)-EYFP expression from a Cre-conditional (floxed-stop) allele (**Fig. 1a**). Optical stimulation of ChR2$^+$ Rbp4 fibers was induced by 5-ms pulses of 473-nm light delivered through the objective while performing voltage-clamp whole-cell recordings from SPNs. AMPA-type glutamate receptor (AMPAR)-mediated currents were isolated by pharmacologically inhibiting NMDA-type glutamate receptors (NMDARs) and $GABA_A$ receptors and recording at a holding potential (V_h) of −70 mV. All of the striatal neurons recorded at P6–7 exhibited oEPSCs (oEPSC amplitude, P6–7, 122 ± 13 pA, n = 16 cells from 2 mice; **Fig. 1b**,**c**), revealing the presence of functional excitatory synapses at these early stages. Evoked current amplitude increased gradually until ~P10 (oEPSC amplitude, P8–9, 181 ± 22 pA, n = 19 cells from 2 mice; P10–11, 595 ± 80 pA, n = 13 cells from 2 mice; **Fig. 1c**) and exhibited a marked increase thereafter (oEPSC amplitude, P12–13, 1848 ± 160 pA, n = 31 cells from 4 mice; P14–15, 3195 ± 146 pA, n = 57 cells from 5 mice, one-way ANOVA, $P < 0.0001$; **Fig. 1c**). To overcome space-clamp limitations caused by large amplitude EPSCs, we performed recordings at later developmental time points at V_h = −20 mV to reduce the electrochemical driving force of AMPAR-mediated ionic currents (**Fig. 1d**). Control recordings at P14 showed a linear relationship between oEPSCs recorded at V_h = −70 and −20 mV across a wide range of amplitudes (**Supplementary Fig. 1**). Evoked oEPSC amplitude increased approximately twofold from P14–15 to P17–18 and stabilized thereafter (P14–15, 731 ± 57 pA, n = 20 cells from 3 mice; P17–18, 1269 ± 59 pA, n = 20 cells from 3 mice; P29–30, 1337 ± 97 pA, n = 19 cells from 3 mice; one-way ANOVA, $P < 0.0001$; **Fig. 1d**,**e**). Normalization across data sets revealed that ~90% of Rbp4$^+$ oEPSC amplitude developed from P8–9 to P17–18 (**Fig. 1e**).

In many brain areas, synapse development is characterized by a gradual recruitment and stabilization of AMPARs resulting in a progressive increase of the ratio of currents carried by AMPARs in relation to NMDARs[26]. To determine the AMPAR/NMDAR current ratio ($R_{A/N}$) in developing SPN synapses we isolated the AMPAR and NMDAR components of oEPSCs by recording at V_h = −70 and +40 mV, respectively (**Fig. 1f**). *Rbp4-Cre;ChR2$^{f/wt}$* mice were used to reduce overall current amplitude and maximize voltage control in the absence of NMDAR inhibitors. There was a significant increase in both the AMPAR (P10–11, 155 ± 24 pA, n = 18 cells from 3 mice; P14–15, 647 ± 65 pA, n = 20 cells from 3 mice; unpaired t test, $P < 0.0001$) and NMDAR (P10–11, 158 ± 19 pA, n = 18; P14–15, 441 ± 45 pA; unpaired t test, $P < 0.0001$) components of oEPSC from P10–11 to P14–15, and $R_{A/N}$ increased significantly during this time period (P10–11, 0.85 ± 0.07, n = 18; P14–15, 1.56 ± 0.14, n = 20, unpaired t test $P = 0.0006$), consistent with ongoing synapse maturation (**Fig. 1g**–**j**)[26,27]. NMDAR EPSC decay kinetics were not significantly different between the two age groups ($P = 0.895$, unpaired t-test; P10–13, τ = 409 ± 40 ms, n = 18; P14–15, τ = 415 ± 23 ms, n = 20; **Fig. 1j**,**k**), suggesting that there is no change in the subunit composition of NMDARs across this developmental period.

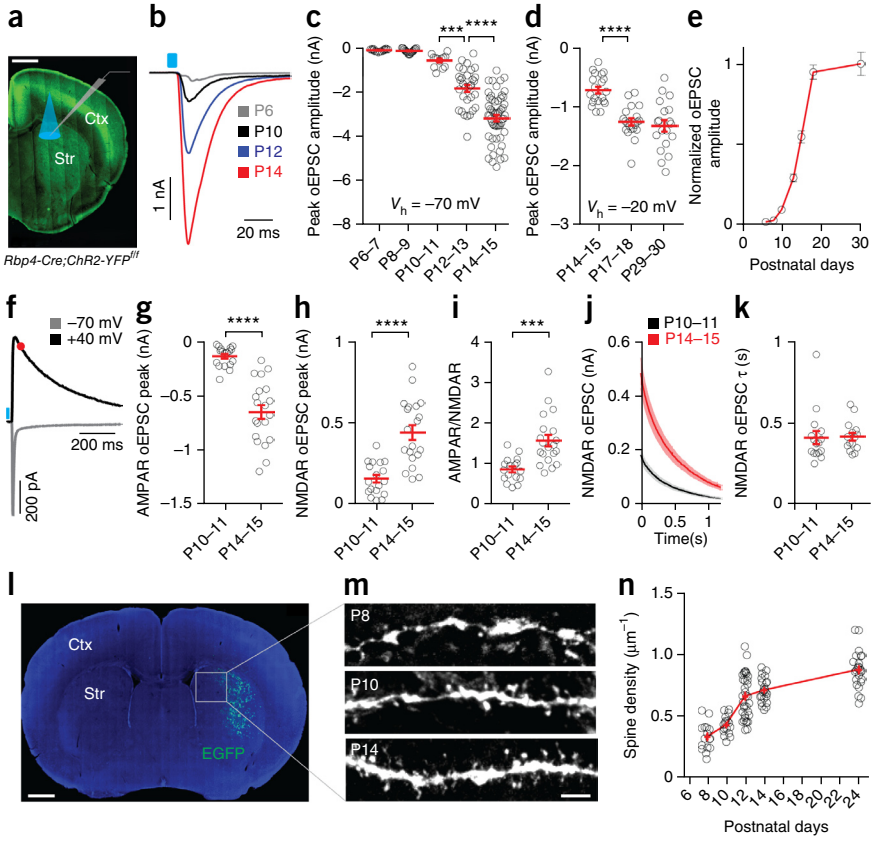

Figure 1 Rapid development of striatal SPN excitatory input in mice after ~P10. (**a**) Whole-cell voltage-clamp recordings in SPNs of dorsomedial striatum in acute brain slices of *Rbp4-Cre;ChR2-YFP$^{f/f}$* mice and optogenetic fiber stimulation using whole-field illumination. Scale bar represents 1 mm. (**b**) AMPAR oEPSCs recorded in SPNs under voltage clamp (V_h = −70 mV) at different postnatal days in response to brief pulses of 473-nm laser light (blue rectangle). (**c**,**d**) Mean oEPSC peak amplitude ± s.e.m. recorded in SPNs at V_h = −70 mV from P6–15 (**c**) and at V_h = −20 mV from P14–30 (**d**). (**e**) Developmental progression of oEPSC amplitude values normalized to P30. Error bars represent normalized s.e.m. (**f**) Representative traces of AMPAR (gray) and NMDAR (black) oEPSCs recorded in the same SPN of *Rbp4-Cre;ChR2-YFP$^{f/wt}$* at V_h = −70 mV and V_h = +40 mV, respectively. Red circle indicates time of NMDAR current amplitude analysis at 50-ms post light stimulus (blue rectangle). (**g**,**h**) Mean AMPAR (**g**) and NMDAR (**h**) oEPSC peak amplitude ± s.e.m. in P10–11 and P14–15 SPNs. (**i**) Mean AMPAR to NMDAR ratio ± s.e.m. for each SPN represented in **g** and **h**. (**j**) Average (solid line) ± s.e.m. (shaded region) NMDAR oEPSCs from cells represented in **g** and **h**. (**k**) Mean NMDAR oEPSC decay time constant (τ) ± s.e.m. of P10–11 and P14–15 SPNs. (**l**) Coronal brain slice of P12 mouse infected with AAV8-CAG-EGFP. Ctx, cortex; Str, striatum. Scale bar represents 1 mm. (**m**) Representative images of EGFP-expressing SPN dendrites at different postnatal days. Scale bar represents 10 μm. (**n**) Average dendritic spine density ± s.e.m. from infected SPNs at P8–24. ***P <0.001; ****P <0.0001.

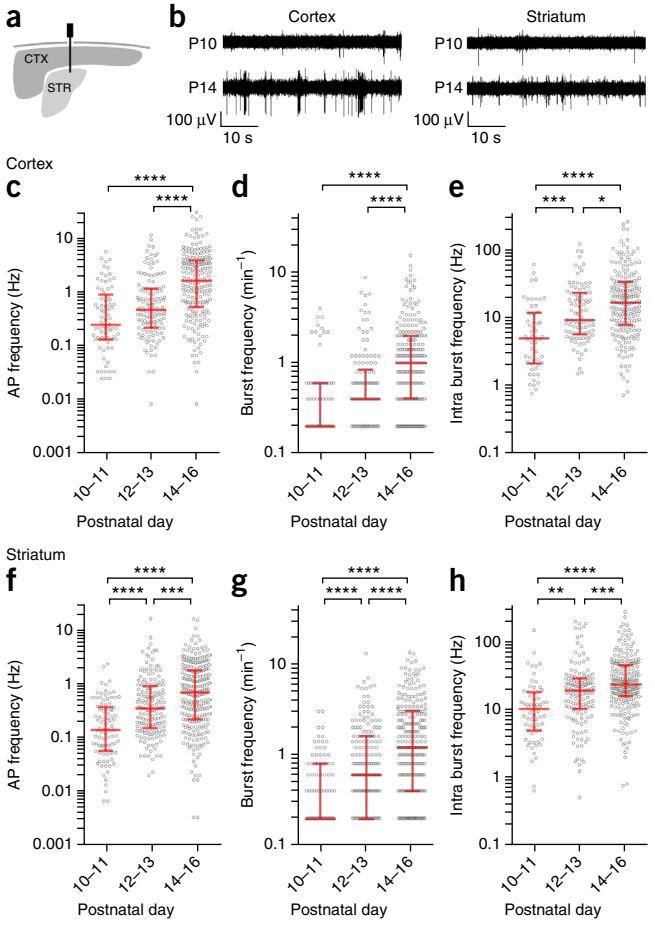

Figure 2 Correlated increase in cortical and striatal activity *in vivo* from P10 to P16. (**a**) Experimental diagram of *in vivo* recordings in a sagittal view of a mouse brain showing cortex (CTX) and striatum (STR). (**b**) Representative recordings of multi-unit activity in cortex (left) and striatum (right) at P10 and P14. (**c**) Median ± interquartile range of average FR of cortical units from P10–11 to P14–16. (**d**,**e**) Median AP burst frequency (**d**) and intra-burst frequency ± interquartile range (**e**) of cortical units shown in **c**. (**f**) Median ± interquartile range of average FR of striatal units at different developmental time points. (**g**,**h**) Median AP burst frequency (**g**) and intra-burst frequency ± interquartile range (**h**) of striatal units shown in **f**. **P* <0.05; ***P* <0.01; ****P* <0.001; *****P* <0.0001.

Corticostriatal synapses are mainly localized in dendritic spines of SPNs[1]. To address whether spinogenesis is associated with oEPSC amplitude increase, we analyzed dendritic spine density in developing SPNs in dorsomedial striatum using adeno-associated virus encoding GFP (AAV8-CAG-EGFP) and confocal microscopy (**Fig. 1l–n**). Consistent with the developmental increase of oEPSC amplitude, the density of spines increased markedly during the second postnatal week, with the highest growth rate between P10 and P12 (P8, $0.33 \pm 0.03\ \mu m^{-1}$, $n = 16$ dendrites from 2 mice; P10, $0.43 \pm 0.02\ \mu m^{-1}$, $n = 17$ dendrites from 2 mice; P12, $0.65 \pm 0.03\ \mu m^{-1}$, $n = 35$ dendrites from 2 mice; P14, $0.71 \pm 0.02\ \mu m^{-1}$, $n = 23$ dendrites from 2 mice; P24, $0.87 \pm 0.03\ \mu m^{-1}$, $n = 25$ dendrites from 2 mice). Together these results indicate that a large fraction of SPN excitatory synapses develops rapidly during the end of the second postnatal week.

Increase in corticostriatal activity *in vivo* from P10–16

To characterize how corticostriatal circuit activity evolves during this period, we recorded multi-unit activity in cortex and striatum of awake head-fixed mice from P10–16 (**Fig. 2a**) following 1-h recovery from surgical headpost implantation. Neuronal activity was recorded using multi-electrode arrays for 20 min after a 10-min stabilization period. Recordings were performed in somatosensory regions of cortex by positioning the electrode array 1,250 µm deep from the surface to target cortical layer 5. The firing rate (FR) of cortical units increased approximately sixfold from P10–16 (median P10–11, 0.25 Hz, $n = 77$ units from 5 mice; P12–13, 0.48 Hz, $n = 125$ units from 5 mice; P14–16, 1.64 Hz, $n = 207$ units from 5 mice; Kruskal-Wallis test, $P < 0.0001$), with a significant increase in the number of bursts fired (median burst frequency P10–11, 0.2 min^{-1}, $n = 77$; P12–13, 0.4 min^{-1}, $n = 125$; P14–16, 1.0 min^{-1}, $n = 207$; Kruskal-Wallis test, $P < 0.0001$) and in the frequency of action potentials (APs) in a burst (median intra burst average frequency P10–11, 4.9 Hz, $n = 53$, $P = 0.035$; P12–13, 9.1 Hz, $n = 89$, $P = 0.0008$; P14–16, 16.4 Hz, $n = 198$, $P < 0.0001$; Kruskal-Wallis test) (**Fig. 2b–e**).

The developmental progression of activity in striatum was similar to cortex with an approximately fivefold increase in average firing rate from P10 to P16 (median FR P10–11, 0.14 Hz, $n = 92$ units from 5 mice; P12–13, 0.36 Hz, $n = 167$ units from 5 mice; P14–16, 0.71 Hz, $n = 255$ units from 5 mice; Kruskal-Wallis test, $P = 0.0007$, $P < 0.0001$) and a significant increase in bursting (median burst frequency, P10–11, 0.2 min^{-1}, $n = 92$; P12–13, 0.6 min^{-1}, $n = 167$; P14–16, 1.2 min^{-1}, $n = 255$; Kruskal-Wallis test, $P < 0.0001$) and intra-burst FR (median intra burst frequency P10–11, 10.0 Hz, $n = 65$; P12–13, 18.7 Hz, $n = 141$; P14–16, 22.8 Hz, $n = 236$, Kruskal-Wallis test, $P = 0.0013$, $P = 0.0002$, $P < 0.0001$) (**Fig. 2f–h**). These results indicate that P10–16 is a period characterized not only by rapid maturation of SPN synapses, but also by a substantial increase in corticostriatal activity.

Corticostriatal coupling during early development

To address whether the observed rise in striatal neuronal activity is caused by the increased number of SPN synapses, we compared responses of striatal neurons to optogenetic stimulation of corticostriatal projection neurons at P10–11 and P14–16. Stimulation of cortical neurons was achieved using *Rbp4-Cre;ChR2$^{f/f}$* mice and extracranial optical stimulation with 473-nm light (**Fig. 3a**). The stimulation protocol consisted of trains of ten pulses at 10 Hz repeated ten times every 30 s, similar to the median AP burst frequency of cortical units at P10–11 (**Fig. 2e**)[28]. Optogenetic stimulation reliably increased the FR of cortical units at all ages (peak FR; P10–11, 11.7 ± 0.5 Hz, $n = 76$ units from 5 mice; P14–16, 14.2 ± 1.3 Hz, $n = 139$ units from 6 mice), with a maximum peak FR in response to the first pulse of the stimulation train (first pulse peak FR; P10–11, 24.6 ± 1.2 Hz; P14–16, 30.9 ± 3.3 Hz) (**Fig. 3d**,**e**). Response latencies were similar in the two age groups with peak FR 5–10 ms after stimulus onset (**Supplementary Fig. 2**). Thus, stimulation of $Rbp4^+$ cortical cells at these two developmental time points increases cortical activity to a similar extent, allowing comparisons of downstream striatal activity across development.

At P14–16, cortical stimulation increased the activity of striatal units (peak FR 12.7 ± 1.3 Hz, $n = 161$ units from 6 mice) with peak responses 15–20 ms after stimulus onset (**Supplementary Fig. 2**). Striatal responses were maximal in response to the first pulse of the train (peak FR in response to first stimulus; P14–16, 29.4 ± 2.6 Hz) and exhibited moderate depression in response to subsequent light flashes (**Fig. 3f**,**g**). However, striatal units also responded strongly to cortical stimulation at P10–11 (post stimulus peak FR; P10–11, 7.9 ± 2.1 Hz, $n = 64$ units from 5 mice) and responded to the first pulse of the stimulation train even more effectively than P14–16 cells (peak FR in response to first stimulus; P10–11, 37.6 ± 5.4 Hz) (**Fig. 3b–g**).

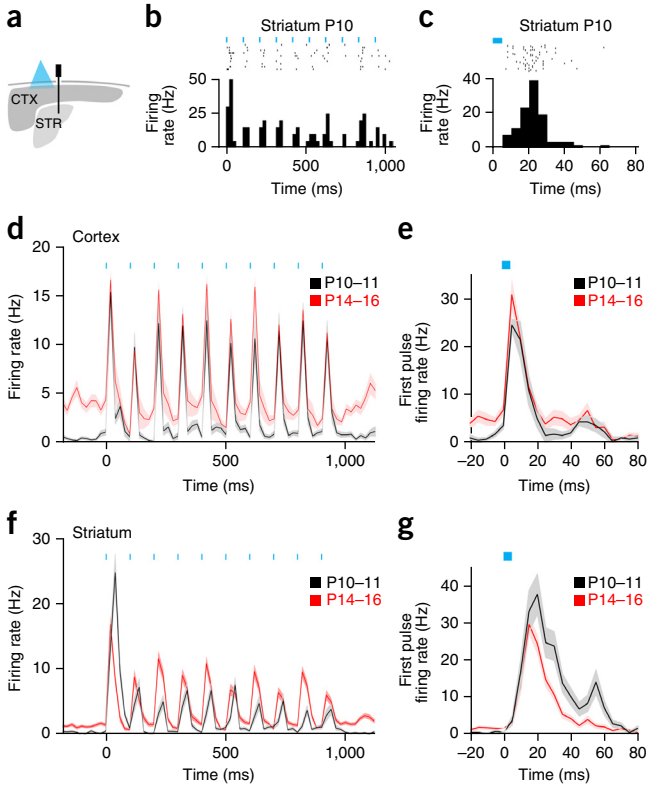

Figure 3 Corticostriatal coupling during early development. (**a**) Experimental diagram of *in vivo* recordings and extracranial optogenetic stimulation using 473-nm laser (blue) in *Rbp4-Cre;ChR2-YFP$^{f/f}$* mice showing cortex (CTX) and striatum (STR). (**b**) Example raster plot (top) and 20-ms bin peri-stimulus time histogram (PSTH, bottom) of action potentials of a P11 striatal unit during optogenetic stimulation of cortex with a 10-Hz light pulse train (blue). Note the robust response to the first pulse of the train. (**c**) Raster plot (top) and 5 ms bin PSTH (bottom) of the unit shown in **b** in response to individual optogenetic pulses (blue). (**d**) PSTH (20-ms bin) representing firing rate of cortical neurons during ChR2 stimulation (blue) at P10–11 (black) and P14–16 (red). Shaded regions represent ± s.e.m. (**e**) PSTH (5-ms bin) of units shown in **d** in response to the first pulse of the stimulation train. Shaded regions represent ± s.e.m. (**f**) PSTH (20-ms bin) of firing rate of striatal neurons during cortical stimulation (blue) at P10–11 (black) and P14–16 (red). Shaded regions represent ± s.e.m. (**g**) PSTH (5-ms bin) of striatal neurons in response to the first pulse of the stimulation train. Shaded regions represent ± s.e.m. Note the presence of secondary peaks indicative of burst firing in response to single light pulses.

Compared with P14–16, P10–11 striatal units exhibited longer 20–25-ms response latencies (**Supplementary Fig. 2**) and more pronounced depression during the stimulation train (**Fig. 3f**). There was no significant difference in pair-pulse ratios (PPRs) of electrically evoked EPSCs (eEPSCs) in SPNs at P9–10 and P15–16 (WT PPR P9, 1.05 ± 0.14, n = 9 neurons from 2 mice; P14, 0.97 ± 0.05, n = 13 neurons from 3 mice; **Supplementary Fig. 3**), suggesting that the increased depression observed at P10–11 is not a result of changes in presynaptic properties of striatal afferents, but may instead be a result of changes in AMPAR desensitization[29,30]. Together, these results reveal that striatal units are already tightly coupled to cortical activity at P10 and can effectively respond to trains of APs.

Increased excitability of SPNs during early development

The robust striatal firing evoked by corticostriatal stimulation at P10–11 appears to be at odds with the much reduced number of SPN excitatory inputs during this early developmental period. To determine whether the early SPN responsivity is a result of increased intrinsic excitability[31], we performed whole-cell recordings in current clamp from SPNs in dorsomedial striatum across development and measured membrane potential changes and AP frequency in response to somatic current injections (**Fig. 4**). The resting membrane potential (V_{rest}) at P10–11 was more depolarized than at later stages (P10–11, −68.7 ± 1.1 mV, n = 26 cells from 3 mice; P13–14, −80.1 ± 0.9 mV, n = 26 cells from 3 mice; P16–17, −80.6 ± 1.4 mV, n = 15 cells from 3 mice; one-way ANOVA, P < 0.0001). In addition, AP firing threshold (P10–11, −29.1 ± 1.3 mV, n = 26; P13–14, −34.5 ± 1.3 mV, n = 26; P16–17, −35.4 ± 0.8 mV, n = 15; one-way ANOVA, P < 0.01) and input resistance (R_i, P10–11, 438 ± 14 MΩ; P12–13, 245 ± 5 MΩ; P16–17, 151 ± 4 MΩ) decreased during this period, whereas rheobase significantly increased with age (P10–11, 93 ± 8 pA; P12–13, 159 ± 11 pA; P16–17, 183 ± 12 pA, one-way ANOVA, P = 0.0002, P < 0.0001). Thus, SPNs undergo extensive maturation of their intrinsic properties and are most excitable during early development.

Precocious SPN maturation in *Shank3B*$^{-/-}$ mice

Shank3B$^{-/-}$ mice display reduced corticostriatal connectivity in adults[23], suggesting that the loss of Shank3 might impair the early development of striatal afferents. We recorded AMPAR mEPSCs from SPNs in dorsomedial striatum of wild-type (WT) and *Shank3B*$^{-/-}$ littermates across development (**Fig. 5a–h**). Because of the rapid rate of cellular and synaptic maturation at these ages, all comparisons were made in litters from mice recorded on the same day. At P10, there was no difference in SPN mEPSC frequency between genotypes (mEPSC frequency; WT, 0.37 ± 0.04 Hz, n = 25 cells from 3 mice; *Shank3B*$^{-/-}$, 0.43 ± 0.05 Hz, n = 27 cells from 3 mice; one-way ANOVA, P > 0.999).

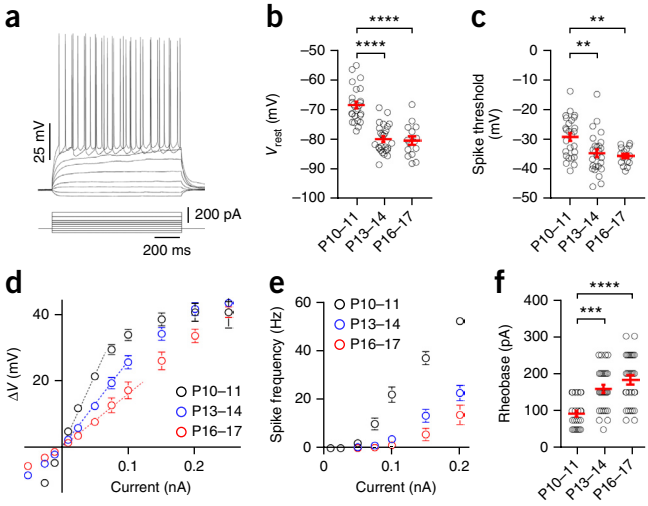

Figure 4 Hyperexcitability of SPNs during early development. (**a**) Example membrane responses to discreet current injection steps in SPNs of dorsomedial striatum. (**b**,**c**) Mean resting membrane potential ± s.e.m. (**b**) and mean spike threshold potential ± s.e.m. (**c**) of SPNs recorded at different postnatal periods. (**d**) Mean ± s.e.m. current-voltage (*I-V*) relationship in SPNs across development. Dashed lines represent linear fits to voltage steps to 10, 25 and 50 pA, whose slopes were used to determine the input resistance. (**e**) Current-firing rate (*I-F*) plot of SPNs across development. Error bars represent ± s.e.m. (**f**) Mean SPN rheobase current ± s.e.m. from P10–11 to P16–17. **P<0.01; ***P<0.001; ****P<0.0001.

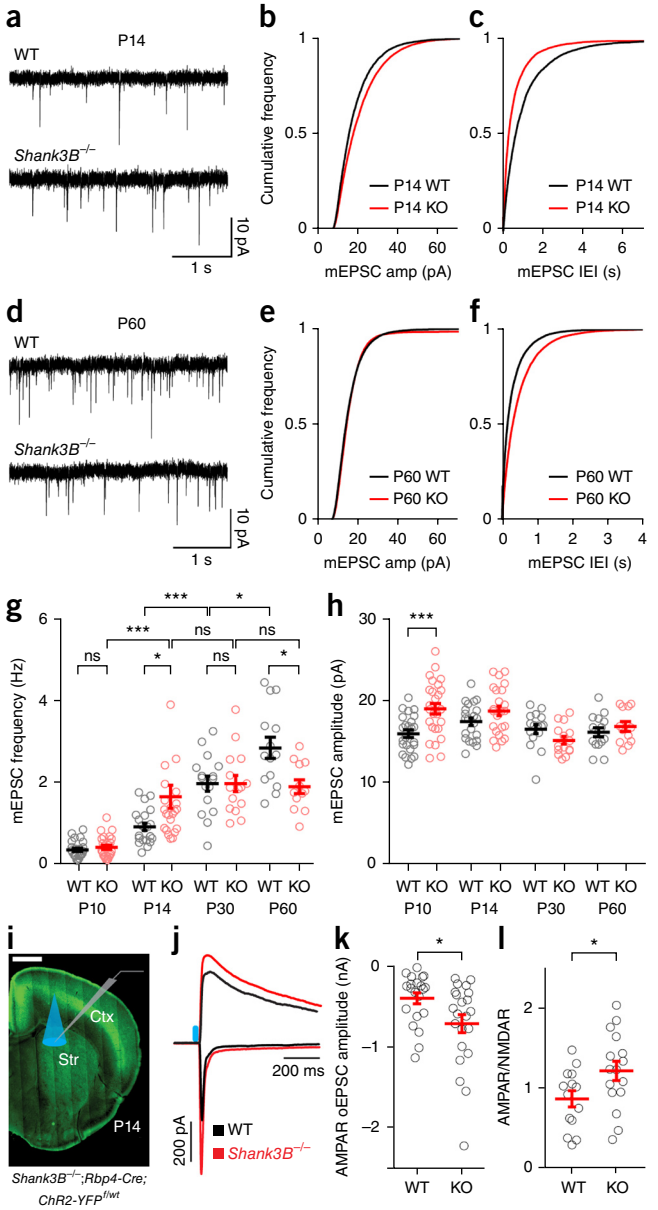

Figure 5 Precocious maturation of striatal glutamatergic inputs in *Shank3B*$^{-/-}$ SPNs. (**a**) Representative mEPSC recordings in SPNs of dorsomedial striatum of WT and *Shank3B*$^{-/-}$ mice at P14. (**b**,**c**) Cumulative distribution of amplitude (**b**) and inter-event interval (**c**) of mEPSCs recorded from SPNs of WT and *Shank3B*$^{-/-}$ littermates at P14. (**d**) Representative mEPSC recordings of WT and *Shank3B*$^{-/-}$ SPNs at P60. (**e**,**f**) Cumulative distribution of amplitude (**e**) and inter-event interval (**f**) of mEPSCs recorded from WT and *Shank3B*$^{-/-}$ littermates at P60. (**g**,**h**) Mean mEPSC frequency (**g**) and amplitude (**h**) ± s.e.m. of SPNs from WT and *Shank3B*$^{-/-}$ animals at different developmental time points. WT maturation was characterized by a continuous increase in mEPSC frequency throughout development, whereas *Shank3B*$^{-/-}$ showed a precocious maturation followed by an arrest in later stages. (**i**) Experimental diagram depicting whole-cell voltage-clamp recordings in SPNs of dorsomedial striatum in acute brain slices of *Shank3B*$^{-/-}$*;Rbp4-Cre;ChR2-YFP*$^{f/wt}$ mice and optogenetic fiber stimulation using whole-field illumination. Scale bar represents 1 mm. (**j**) Representative average AMPAR and NMDAR oEPSCs from WT (black) and *Shank3B*$^{-/-}$ (red) SPNs. Blue rectangle represents 5-ms 473-nm light stimulation. (**k**) Mean AMPAR oEPSC peak amplitude ± s.e.m. in P14 WT and KO SPNs. (**l**) Mean AMPAR to NMDAR ratio ± s.e.m. for SPNs represented in **k**. **P* <0.05; ****P* <0.001; ns, *P* ≥ 0.95.

However, at P14, *Shank3B*$^{-/-}$ SPNs had elevated mEPSC frequency compared with WT controls (mEPSC frequency; WT, 0.93 ± 0.09 Hz, *n* = 21 cells from 4 mice; *Shank3B*$^{-/-}$, 1.71 ± 0.29 Hz, *n* = 22 cells from 4 mice; one-way ANOVA, *P* = 0.015). Furthermore, whereas in control mice the rate of SPN mEPSC increased gradually until adulthood, in *Shank3B*$^{-/-}$ mice it plateaued at P30 (P30 WT, 1.97 ± 0.18 Hz, *n* = 16 cells from 3 mice; P30 *Shank3B*$^{-/-}$, 1.98 ± 0.20, *n* = 15 cells from 3 mice; P60 WT, 2.84 ± 0.26 Hz, *n* = 15 cells from 3 mice; P60 *Shank3B*$^{-/-}$, 2.00 ± 0.19 Hz, *n* = 12 cells from 3 mice). Notably, *Shank3B*$^{-/-}$ SPNs exhibited significantly increased mEPSC amplitude relative to WT controls at P10, but not at any later stages (P10 WT, 16 ± 1; *Shank3B*$^{-/-}$, 19 ± 1 pA; one-way ANOVA, *P* = 0.0009; P14 WT 18 ± 1 pA; *Shank3B*$^{-/-}$, 19 ± 1 pA; P30 WT, 17 ± 1 pA; *Shank3B*$^{-/-}$, 15 ± 1 pA; P60 WT, 16 ± 1 pA; *Shank3B*$^{-/-}$, 17 ± 1 pA). PPR of eEPSC was not significantly different between genotypes at P14 (*P* = 0.287, unpaired *t*-test; WT, 0.97 ± 0.05, *n* = 13 cells from 2 mice; *Shank3B*$^{-/-}$, 1.04 ± 0.04, *n* = 14 cells from 2 mice; **Supplementary Fig. 3b**), suggesting that the higher mEPSC frequency observed in *Shank3B*$^{-/-}$ SPNs is not a result of altered release probability.

To compare overall excitatory drive onto WT and *Shank3B*$^{-/-}$ SPNs, we measured AMPAR and NMDAR oEPSCs in dorsomedial striatum of mice expressing Rbp4-Cre and ChR2 (*Shank3*$^{-/-}$*;Rbp-Cre;ChR2*$^{f/wt}$) (**Fig. 5i–l**). Rbp4^{+} oEPSC amplitude was increased in *Shank3B*$^{-/-}$ SPNs compared with WT at P13–14 (WT, 399 ± 68 pA, *n* = 21 cells from 3 mice; *Shank3B*$^{-/-}$, 710 ± 110 pA, *n* = 22 cells from 3 mice; unpaired *t* test, *P* = 0.022). This relative difference was also observed between heterozygote and *Shank3B*$^{-/-}$ mice (*Shank3B*$^{+/-}$, 386 ± 48 pA, *n* = 37 cells from 3 mice; *Shank3B*$^{-/-}$, 541 ± 45 pA, *n* = 40 cells from 3 mice; unpaired *t* test *P* = 0.021; **Supplementary Fig. 4**). The increase in AMPAR oEPSC amplitude in *Shank3B*$^{-/-}$ SPNs also resulted in increased $R_{A/N}$ (oEPSC $R_{A/N}$ WT, 0.86 ± 0.01, *n* = 14; *Shank3B*$^{-/-}$, 1.21 ± 0.12, *n* = 16; unpaired *t* test, *P* = 0.036), consistent with a larger fraction of synapses exhibiting AMPAR currents in relation to controls. Taken together, these results show a premature increase and subsequent arrest in the development of SPN excitatory inputs in *Shank3B*$^{-/-}$ mice when compared with WT.

Early corticostriatal hyperactivity in *Shank3B*$^{-/-}$ mice

To characterize corticostriatal circuit activity in *Shank3B*$^{-/-}$ mice during early development, we performed multi-unit recordings in cortex and dorsomedial striatum of awake P13–14 WT and *Shank3B*$^{-/-}$ littermates (**Fig. 6a–f**). Cortical activity was elevated in *Shank3B*$^{-/-}$ animals approximately twofold compared with WT (median FR, WT, 0.73 Hz, *n* = 154 units from 4 mice; *Shank3B*$^{-/-}$, 1.34 Hz, *n* = 155 units from 4 mice; Mann Whitney *U* test, *P* = 0.0006). The frequency of cortical AP bursts was not statistically different between genotypes, but the intra-burst average FR was significantly increased in the cortex of *Shank3B*$^{-/-}$ animals (median burst frequency: WT, 0.8 min^{-1}, *n* = 154; *Shank3B*$^{-/-}$, 0.8 min^{-1}, *n* = 155; median intra-burst frequency: WT, 13.8 Hz, *n* = 102; *Shank3B*$^{-/-}$, 27.9 Hz, *n* = 121; Mann Whitney *U* test, *P* < 0.0001).

Notably, striatal activity was also increased in *Shank3B*$^{-/-}$ mice compared with WT (median FR: WT, 0.27 Hz, *n* = 155 units from 4 mice; *Shank3B*$^{-/-}$, 0.48 Hz, *n* = 144 units from 4 mice; Mann Whitney *U* test, *P* = 0.002). Moreover, in striatum of *Shank3B*$^{-/-}$ mice, the frequency of AP bursts (median burst frequency: WT, 0.6 min^{-1}, *n* = 155; *Shank3B*$^{-/-}$, 1.2 min^{-1}, *n* = 144; Mann Whitney *U* test, *P* < 0.0001) and the intra-burst AP frequency (median intra burst frequency: WT, 16.85 Hz, *n* = 125; *Shank3B*$^{-/-}$, 20.53 Hz, *n* = 138; Mann Whitney *U P* = 0.0209) were also increased (**Fig. 6g–i**).

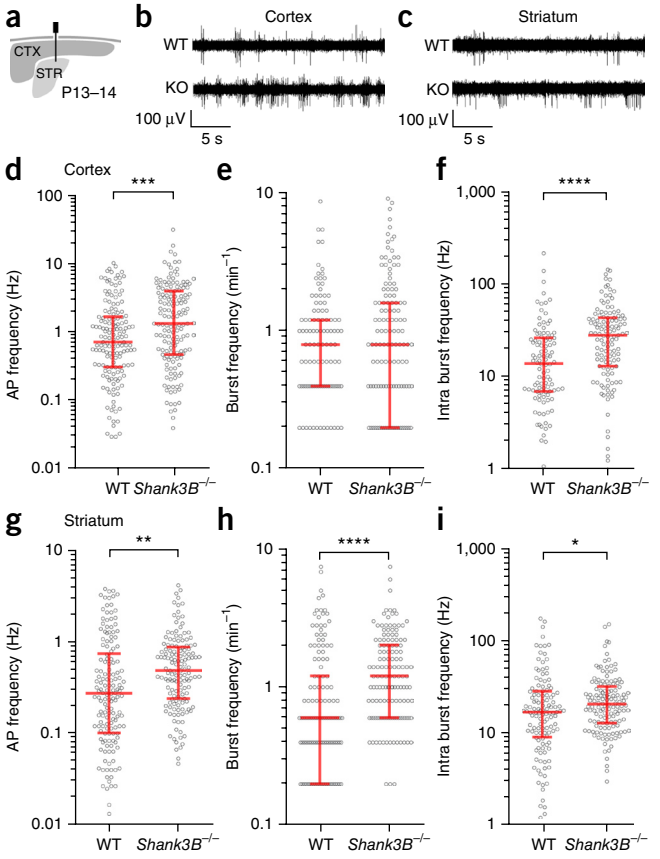

Figure 6 Cortical hyperactivity in neonatal *Shank3B*$^{-/-}$ mice. (**a**) Experimental diagram of *in vivo* recordings in a sagittal view of a mouse brain showing cortex (CTX) and striatum (STR). (**b**,**c**) Representative recordings of multi-unit activity in cortex (**b**) and striatum (**c**) of WT and *Shank3B*$^{-/-}$ animals at P13–14. (**d**) Median ± interquartile range of average FR of cortical units from WT and *Shank3B*$^{-/-}$ mice. (**e**,**f**) Median frequency of AP bursts (**e**) and intra-burst frequency ± interquartile range (**f**) of cortical units shown in **d**. (**g**) Median ± interquartile range of average FR of striatal units from WT and *Shank3B*$^{-/-}$ mice. (**h**,**i**) Median frequency of AP bursts (**h**) and intra-burst firing rate ± interquartile range (**i**) of cortical units shown in **e**. $^{*}P<0.05$; $^{**}P<0.01$; $^{***}P<0.001$; $^{****}P<0.0001$.

We detected no difference in SPN R_i, V_{rest}, rheobase or spike threshold potential between genotypes (V_{rest}, WT, −79.3 ± 2.4 mV; *Shank3B*$^{-/-}$, −81.5 ± 1.8 mV; spike threshold, WT, −38.0 ± 0.8 mV; *Shank3B*$^{-/-}$, −37.4 ± 1.0 mV; rheobase, WT, −155 ± 19 pA; *Shank3B*$^{-/-}$, 175 ± 17 pA; **Supplementary Fig. 5**), indicating that increased striatal activity observed in knockout animals is not a result of the increased SPN excitability.

Cortical activity drives corticostriatal connectivity

To directly test whether elevated cortical activity can increase corticostriatal connectivity, we silenced cortical GABAergic interneuron output by conditional deletion of the vesicular GABA transporter (vGAT) in *Slc32a1*$^{f/f}$ transgenic mice. Recombination was achieved by unilateral injection of AAVs expressing Cre recombinase under the control of the neuron-specific synapsin promoter (AAV-Syn-Cre-GFP) in frontal, motor and somatosensory cortex at P3–4 (**Fig. 7a**). Injected animals did not present signs of seizures, but exhibited epileptiform spike and wave activity patterns in local field potential recordings of injected cortical regions (**Fig. 7b**,**c**) and overall movement deficits in an open chamber test (distance moved: control, 1.70 ± 0.40 m; Cre injected, 0.84 ± 0.21 m; *t* test, $P = 0.044$; velocity: control, 1.96 ± 0.37 cm s^{-1}; Cre injected, 0.99 ± 0.20 cm s^{-1}; *t* test, $P = 0.037$; time moving: control, 244.5 ± 66.3 s; Cre injected, 109.7 ± 32.8 s; *t* test, $P = 0.040$, $n = 4$ mouse pairs; **Supplementary Fig. 6**).

SPNs in dorsomedial striatum of injected P12–14 *vGAT*$^{f/f}$ animals had twofold higher mEPSC frequency than controls (control, 0.63 ± 0.06 Hz, $n = 17$ cells from 3 mice; Cre injected, 1.27 ± 0.17, $n = 16$ cells from 3 mice; *t* test, $P = 0.001$; **Fig. 7d–h**), with no significant change in mEPSC amplitude ($P = 0.218$, unpaired *t*-test; control, 19 ± 1 pA, $n = 17$; Cre injected, 21 ± 1, $n = 16$). PPRs of eEPSCs were not statistically different between experimental groups (eEPSC PPR; control, 0.90 ± 0.09, $n = 10$ cells from 2 mice; Cre injected, 1.06 ± 0.12, $n = 9$ cells from 2 mice; **Supplementary Fig. 7**), indicating that the increase in mEPSC frequency was likely not a result of altered vesicular release probability.

To test whether increased cortical activity can acutely alter corticostriatal connectivity we performed extracranial optogenetic stimulation of corticostriatal projections from frontal regions of cortex by implanting a lightweight 470-nm LED unilaterally onto the skull of P10–11 of *Rbp4-Cre;ChR2*$^{f/f}$ mice[32] (**Fig. 7i**). Mice were stimulated with five pulses at 10 Hz every minute for 1 h corresponding to a ~25% net increase over basal cortical AP firing and an approximately fivefold increase in AP burst frequency (**Fig. 2c**,**d**). Acute brain slices were prepared immediately after stimulation and AMPAR-mediated oEPSCs were measured from SPNs located in dorsomedial striatum of the ipsilateral (stimulated) or contralateral (control) hemisphere (**Fig. 7j–l**). Ipsilateral SPNs exhibited elevated oEPSC amplitude compared with contralateral controls (average oEPSC amplitude; ipsilateral, 737 ± 63 pA, $n = 26$ cells from 4 mice; contralateral, 532 ± 67 pA, $n = 25$ cells from 4 mice; *t* test $P = 0.031$) and this relationship was found in all mouse pairs studied (mean difference of oEPSC amplitude: 200 ± 39 pA, $n = 4$ mice, paired *t* test $P = 0.014$). These results indicate that elevated cortical activity during early development rapidly enhances SPN excitatory input and suggest that the corticostriatal circuit abnormalities observed in developing *Shank3B*$^{-/-}$ mice may be secondary to increased cortical activity.

Decreasing cortical activity rescues *Shank3B*$^{-/-}$ phenotype

To directly test whether the abnormal development of striatal connectivity observed in *Shank3B*$^{-/-}$ mice is caused by cortical hyperactivity, we reduced cortical activity during development and measured AMPAR mEPSCs in SPNs at P13–14. To gain spatio-temporal control over the activity of layer 5 corticostriatal projecting neurons, we bilaterally injected AAVs expressing Cre-dependent G_i-coupled inhibitory DREADD (hM4D$_i$-mCherry) into the cortex of *Shank3B*$^{-/-}$;*Rbp4-Cre* animals during the first postnatal days. This strategy resulted in expression of hM4D$_i$ exclusively in Rbp4^{+} layer 5 cortical cells (**Fig. 8a**,**b**). Clozapine *N*-oxide (CNO, 1 mg per kg of body weight) was administered subcutaneously twice a day for 3 d to activate hM4D$_i$ and decrease corticostriatal activity. SPNs of *Shank3B*$^{-/-}$;*Rbp4-Cre* animals injected with CNO had lower mEPSC frequency than saline injected controls (mEPSC frequency: saline, 1.23 ± 0.1 Hz, $n = 25$ neurons from 3 mice; CNO, 0.78 ± 0.07 Hz, $n = 24$ neurons from 3 mice; unpaired *t* test, $P = 0.0006$; mEPSC amplitude: saline, 17 ± 1 pA; CNO, 17 ± 1 pA; **Fig. 8c–e**).

DISCUSSION

Despite evidence implicating BG dysfunction in neurodevelopmental disorders, the rules underlying the early development of subcortical circuits and the contribution of these processes to human disease

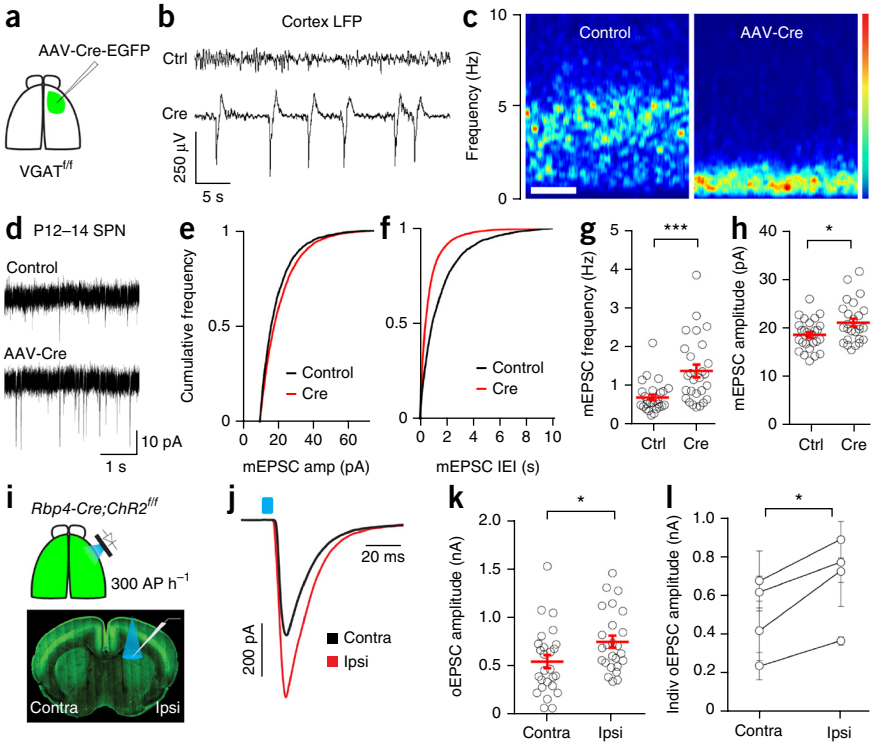

Figure 7 Elevated cortical activity during early development increases corticostriatal connectivity. (**a**) Silencing of cortical interneuron output was achieved by injecting Cre-expressing adenovirus in the cortex of *Slc32a1*$^{f/f}$ animals at P4. (**b**) Local field potential (LFP) recordings from cortex of control and AAV-injected animals at P14 show epileptiform patterns of activity after VGAT deletion. (**c**) Spectrogram of LFPs shown in **b**. Scale bar represents 1 min. Color scale represents normalized power. (**d**) Example mEPSC recordings in SPNs of dorsomedial striatum of control and AAV-Cre–injected animals. (**e**,**f**) Cumulative distribution of mEPSC amplitude (**e**) and mEPSC inter-event interval values (**f**) for the total pool of mEPSCs recorded from control (black) and Cre-injected (red) littermates at P12–14. (**g**,**h**) Cell average mEPSC frequency (**g**) and amplitude ± s.e.m. (**h**) of SPNs from control and Cre-injected animals. (**i**) Schematic showing optogenetic cortical stimulation using extracranial implant of a low mass LED (blue) in *Rbp4-Cre;ChR2*$^{f/f}$ animals (top) and subsequent oEPSC measurements in SPNs in the ipsilateral (stimulated) and contralateral (control) hemispheres (bottom). (**j**) Example AMPAR oEPSCs recorded in SPNs located in dorsomedial striatum of the stimulated (ipsi, red) or opposite (contra, black) hemisphere in response to 5-ms pulses of 473-nm laser light (blue rectangle). (**k**) Mean oEPSC amplitude ± s.e.m. of control (contra) and stimulated (ipsi) SPNs. (**l**) Pair-wise comparison of average oEPSC amplitude in animals recorded in **k**. Error bars represent s.e.m. **P* <0.05; ****P* <0.001.

remain unclear. In mice, glutamatergic afferents innervate striatum at P3–4 (ref. 33), and we found that they evoked synaptic responses in SPNs by P6, indicating that SPN synaptogenesis starts soon after axon innervation. The development of SPN excitatory inputs progresses gradually up to ~P10 and undergoes a period of rapid maturation from P10–18. This period of accelerated synaptogenesis is accompanied by a significant increase in cortical and striatal neuronal activity, possibly as a result of maturation of sensory systems and increases in thalamocortical input[34,35]. Nevertheless, our results indicate that, despite the much reduced corticostriatal drive and synapse density of immature SPNs, striatum can respond to cortical activity at P10. This early responsivity was, at least in part, a result of elevated SPN V_{rest} and R_i that decreased progressively during development, similar to other neuronal cell types[36]. These adaptations likely arise from changes in ion channel expression that optimally tune neuron responses to early patterns of activity[31,37] and contribute to activity-dependent maturation of sensorimotor circuits during early postnatal periods[38]. Moreover, the tight functional coupling of cortex and striatum suggests that early imbalances in cortical activity can alter the trajectory of corticostriatal circuit maturation. Indeed, we found elevated cortical activity and both SPN mEPSC frequency and oEPSC amplitude in P13–14 *Shank3B*$^{-/-}$ SPNs compared with WT. Notably, this phenotype was rescued by chemogenetic reduction of cortical activity, indicating that it is secondary to cortical hyper-activity. Moreover, this finding is unexpected, as adult *Shank3B*$^{-/-}$ mice have reduced corticostriatal drive[23] and Shank3 expression levels are correlated with glutamatergic synapse strength and number in several other *in vivo* and *in vitro* systems[14,17,18,21–24,39].

A recent study reported decreased number of parvalbumin-expressing terminals in cortex of *Shank3B*$^{-/-}$ mice[40]. Given the large increase in thalamocortical afferent activity during early development[34,36,38], decreased inhibition could result in cortical hyper-activity, which would in turn enhance corticostriatal synaptogenesis. This hypothesis is consistent with the increase in SPN mESPC frequency resulting from either vGAT deletion in cortex or acute optogenetic stimulation of corticostriatal projection neurons. Moreover, these results indicate that both chronic and acute periods of elevated cortical activity can increase corticostriatal connectivity.

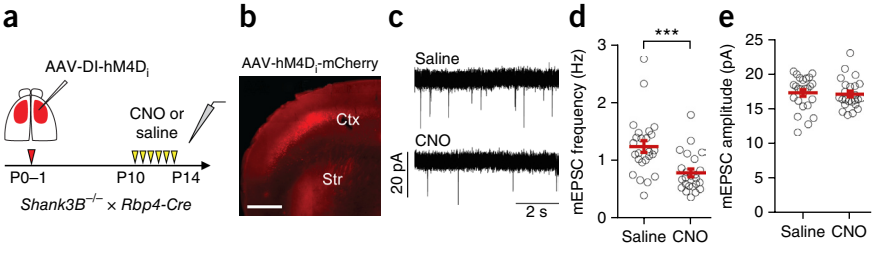

Figure 8 Early increase in corticostriatal drive in *Shank3B*$^{-/-}$ mice is a result of cortical hyperactivity. (**a**) Schematic representing bilateral injection of AAV8-DI-hM4D$_i$ into cortex of *Shank3B*$^{-/-}$;*Rbp4-Cre* mice at P1–2 and bi-daily administration of CNO for 3 d before mEPSC recordings at P13–14. (**b**) Coronal brain slice of P13 *Shank3B*$^{-/-}$;*Rbp4-Cre* mouse infected with AAV8-DI-hM4D$_i$-mCherry. Ctx, cortex; Str, striatum. Scale bar represents 1 mm. (**c**) Example mEPSC recordings in SPNs of dorsomedial striatum of saline- or CNO-injected animals. (**d**,**e**) Cell average mEPSC frequency (**d**) and amplitude (**e**) ± s.e.m. of SPNs of saline- or CNO-injected animals ****P* <0.001.

Although the ontogeny of BG circuits in humans remains unknown, the maturation of SPNs in rhesus monkeys occurs gradually throughout the first year of life, which is analogous to the toddler/preschool stage in humans[3,41]. Autistic individuals share a core set of behavioral symptoms, suggesting that the multiple genetic abnormalities underlying ASDs may converge onto common neurological mechanisms. Notably, one third of autistic individuals develop seizures during infancy and an even larger fraction exhibit subclinical forms of epileptiform activity[42], consistent with the cortical hyperactivity exhibited by several transgenic mouse lines carrying ASD-associated gene mutations[40,43–46].

Our results indicate that, in mice, abnormal hyperactivity of corticostriatal afferents during a period of high SPN excitability alters the normal course of BG circuit development. If similar activity-dependent rules are conserved in humans, this anomalous developmental pattern could help explain why children with autism develop repetitive behaviors and often present precocious maturation and posterior regression of certain cognitive abilities. It is important to note that *Shank3B*$^{-/-}$ mice only exhibit autistic-like behaviors such as over-grooming during adulthood, and the relationship between the early phenotype described here and the onset of these behaviors remains unknown. However, repetitive behaviors in autistic children emerge during the first 2 years of age[47,48] and often become persistent throughout life[49]. Likewise, motor stereotypies associated with ADHD, OCD and Tourette syndrome exhibit a similar early developmental onset[50], suggesting that they are established during the early stages of BG circuit development. Thus, in addition to providing an experimental framework for characterizing circuit formation and cross-circuit interactions during mouse development, our results reveal mechanisms that may be implicated in the pathophysiology of multiple neurodevelopmental disorders.

METHODS

Methods and any associated references are available in the online version of the paper.

Note: Any Supplementary Information and Source Data files are available in the online version of the paper.

ACKNOWLEDGMENTS

We thank I. Oldenburg for help with *in vivo* recordings and analysis and J. Levasseur and R. Pemberton for mouse genotyping and colony management. We thank S. da Silva, C. Deister and the members of the Sabatini laboratory for helpful discussions and critical reading of the manuscript. R.T.P. was supported by the Alice and Joseph Brooks fellowship and the Nancy Lurie Marks clinical and research fellowship in autism. Y.K. was supported by the Leonard and Isabelle Goldenson Research Fellowship and the Nancy Lurie Marks Family Foundation. This work was supported by the National Institute of Neurological Disorders and Stroke (NS046579, to B.L.S.) and the Nancy Lurie Marks Foundation.

AUTHOR CONTRIBUTIONS

R.T.P. and B.L.S. conceived the study and wrote the manuscript. R.T.P. carried out *in vivo* recordings and analyzed the data. R.T.P., W.W. and Y.K. carried out *in vitro* slice recordings and R.T.P. analyzed the data. D.M.C. performed the behavioral experiments and dendritic spine imaging and analysis.

COMPETING FINANCIAL INTERESTS

The authors declare no competing financial interests.

1. Shepherd, G.M.G. Corticostriatal connectivity and its role in disease. *Nat. Rev. Neurosci.* **14**, 278–291 (2013).
2. Oldenburg, I.A. & Sabatini, B.L. Antagonistic but not symmetric regulation of primary motor cortex by basal ganglia direct and indirect pathways. *Neuron* **86**, 1174–1181 (2015).
3. Difiglia, M., Pasik, P. & Pasik, T. Early postnatal development of the monkey neostriatum: a Golgi and ultrastructural study. *J. Comp. Neurol.* **190**, 303–331 (1980).
4. Levine, M.S., Fisher, R.S., Hull, C.D. & Buchwald, N.A. Postnatal development of identified medium-sized caudate spiny neurons in the cat. *Brain Res.* **389**, 47–62 (1986).
5. Tepper, J.M., Sharpe, N.A., Koós, T.Z. & Trent, F. Postnatal development of the rat neostriatum: electrophysiological, light- and electron-microscopic studies. *Dev. Neurosci.* **20**, 125–145 (1998).
6. Kozorovitskiy, Y., Saunders, A., Johnson, C.a., Lowell, B.B. & Sabatini, B.L. Corrigendum: Recurrent network activity drives striatal synaptogenesis. *Nature* **489**, 326–326 (2012).
7. Langen, M., Durston, S., Staal, W.G., Palmen, S.J.M.C. & van Engeland, H. Caudate nucleus is enlarged in high-functioning medication-naive subjects with autism. *Biol. Psychiatry* **62**, 262–266 (2007).
8. Wolff, J.J., Hazlett, H.C., Lightbody, A.A., Reiss, A.L. & Piven, J. Repetitive and self-injurious behaviors: associations with caudate volume in autism and fragile X syndrome. *J. Neurodev. Disord.* **5**, 12 (2013).
9. Langen, M. *et al.* Changes in the developmental trajectories of striatum in autism. *Biol. Psychiatry* **66**, 327–333 (2009).
10. Langen, M. *et al.* Changes in the development of striatum are involved in repetitive behavior in autism. *Biol. Psychiatry* **76**, 405–411 (2014).
11. Lord, C., Cook, E.H., Leventhal, B.L. & Amaral, D.G. Autism spectrum disorders. *Neuron* **28**, 355–363 (2000).
12. DeLong, M. & Wichmann, T. Changing views of basal ganglia circuits and circuit disorders. *Clin. EEG Neurosci.* **41**, 61–67 (2010).
13. Abrahams, B.S. & Geschwind, D.H. Advances in autism genetics: on the threshold of a new neurobiology. *Nat. Rev. Genet.* **9**, 341–355 (2008).
14. Jiang, Y.H. & Ehlers, M.D. Modeling autism by SHANK gene mutations in mice. *Neuron* **78**, 8–27 (2013).
15. Durand, C.M. *et al.* Mutations in the gene encoding the synaptic scaffolding protein SHANK3 are associated with autism spectrum disorders. *Nat. Genet.* **39**, 25–27 (2007).
16. Gauthier, J. *et al.* Novel de novo SHANK3 mutation in autistic patients. *Am. J. Med. Genet. B. Neuropsychiatr. Genet.* **150B**, 421–424 (2009).
17. Roussignol, G. *et al.* Shank expression is sufficient to induce functional dendritic spine synapses in aspiny neurons. *J. Neurosci.* **25**, 3560–3570 (2005).
18. Arons, M.H. *et al.* Autism-associated mutations in ProSAP2/Shank3 impair synaptic transmission and neurexin-neuroligin-mediated transsynaptic signaling. *J. Neurosci.* **32**, 14966–14978 (2012).
19. Han, K. *et al.* SHANK3 overexpression causes manic-like behavior with unique pharmacogenetic properties. *Nature* **503**, 72–77 (2013).
20. Verpelli, C. *et al.* Importance of Shank3 protein in regulating metabotropic glutamate receptor 5 (mGluR5) expression and signaling at synapses. *J. Biol. Chem.* **286**, 34839–34850 (2011).
21. Bozdagi, O. *et al.* Haploinsufficiency of the autism-associated Shank3 gene leads to deficits in synaptic function, social interaction and social communication. *Mol. Autism* **1**, 15 (2010).
22. Yang, M. *et al.* Reduced excitatory neurotransmission and mild autism-relevant phenotypes in adolescent Shank3 null mutant mice. *J. Neurosci.* **32**, 6525–6541 (2012).
23. Peça, J. *et al.* Shank3 mutant mice display autistic-like behaviours and striatal dysfunction. *Nature* **472**, 437–442 (2011).
24. Wang, X. *et al.* Synaptic dysfunction and abnormal behaviors in mice lacking major isoforms of Shank3. *Hum. Mol. Genet.* **20**, 3093–3108 (2011).
25. Harris, J.A. *et al.* Anatomical characterization of Cre driver mice for neural circuit mapping and manipulation. *Front. Neural Circuits* **8**, 76 (2014).
26. Petralia, R.S. *et al.* Selective acquisition of AMPA receptors over postnatal development suggests a molecular basis for silent synapses. *Nat. Neurosci.* **2**, 31–36 (1999).
27. Busetto, G., Higley, M.J. & Sabatini, B.L. Developmental presence and disappearance of postsynaptically silent synapses on dendritic spines of rat layer 2/3 pyramidal neurons. *J. Physiol. (Lond.)* **586**, 1519–1527 (2008).
28. Khazipov, R. *et al.* Early motor activity drives spindle bursts in the developing somatosensory cortex. *Nature* **432**, 758–761 (2004).
29. Carter, A.G., Soler-Llavina, G.J. & Sabatini, B.L. Timing and location of synaptic inputs determine modes of subthreshold integration in striatal medium spiny neurons. *J. Neurosci.* **27**, 8967–8977 (2007).
30. Choi, S. & Lovinger, D.M. Decreased probability of neurotransmitter release underlies striatal long-term depression and postnatal development of corticostriatal synapses. *Proc. Natl. Acad. Sci. USA* **94**, 2665–2670 (1997).
31. Moody, W.J. & Bosma, M.M. Ion channel development, spontaneous activity, and activity-dependent development in nerve and muscle cells. *Physiol. Rev.* **85**, 883–941 (2005).
32. Kozorovitskiy, Y. *et al.* Neuromodulation of excitatory synaptogenesis in striatal development. *eLife* **4**, e10111 (2015).
33. Sohur, U.S., Padmanabhan, H.K., Kotchetkov, I.S., Menezes, J.R.L. & Macklis, J.D. Anatomic and molecular development of corticostriatal projection neurons in mice. *Cereb. Cortex* **24**, 293–303 (2014).
34. Colonnese, M.T. *et al.* A conserved switch in sensory processing prepares developing neocortex for vision. *Neuron* **67**, 480–498 (2010).
35. Kilb, W., Kirischuk, S. & Luhmann, H.J. Electrical activity patterns and the functional maturation of the neocortex. *Eur. J. Neurosci.* **34**, 1677–1686 (2011).
36. Etherington, S.J. & Williams, S.R. Postnatal development of intrinsic and synaptic properties transforms signaling in the layer 5 excitatory neural network of the visual cortex. *J. Neurosci.* **31**, 9526–9537 (2011).

37. Gertler, T.S., Chan, C.S. & Surmeier, D.J. Dichotomous anatomical properties of adult striatal medium spiny neurons. *J. Neurosci.* **28**, 10814–10824 (2008).
38. Kirkby, L.A., Sack, G.S., Firl, A. & Feller, M.B. A role for correlated spontaneous activity in the assembly of neural circuits. *Neuron* **80**, 1129–1144 (2013).
39. Grabrucker, A.M. *et al.* Concerted action of zinc and ProSAP/Shank in synaptogenesis and synapse maturation. *EMBO J.* **30**, 569–581 (2011).
40. Gogolla, N., Takesian, A.E., Feng, G., Fagiolini, M. & Hensch, T.K. Sensory integration in mouse insular cortex reflects GABA circuit maturation. *Neuron* **83**, 894–905 (2014).
41. Martin, L.J. & Cork, L.C. The non-human primate striatum undergoes marked prolonged remodeling during postnatal development. *Front. Cell. Neurosci.* **8**, 294 (2014).
42. Lewine, J.D. *et al.* Magnetoencephalographic patterns of epileptiform activity in children with regressive autism spectrum disorders. *Pediatrics* **104**, 405–418 (1999).
43. Gonçalves, J.T., Anstey, J.E., Golshani, P. & Portera-Cailliau, C. Circuit level defects in the developing neocortex of Fragile X mice. *Nat. Neurosci.* **16**, 903–909 (2013).
44. Bateup, H.S. *et al.* Excitatory/inhibitory synaptic imbalance leads to hippocampal hyperexcitability in mouse models of tuberous sclerosis. *Neuron* **78**, 510–522 (2013).
45. Peñagarikano, O. *et al.* Absence of CNTNAP2 leads to epilepsy, neuronal migration abnormalities, and core autism-related deficits. *Cell* **147**, 235–246 (2011).
46. Han, S. *et al.* Autistic-like behaviour in Scn1a$^{+/-}$ mice and rescue by enhanced GABA-mediated neurotransmission. *Nature* **489**, 385–390 (2012).
47. Wolff, J.J. *et al.* Longitudinal patterns of repetitive behavior in toddlers with autism. *J. Child Psychol. Psychiatry* **55**, 945–953 (2014).
48. Goldman, S. *et al.* Motor stereotypies in children with autism and other developmental disorders. *Dev. Med. Child Neurol.* **51**, 30–38 (2009).
49. Goldman, S. & Greene, P.E. Stereotypies in autism: a video demonstration of their clinical variability. *Front. Integr. Neurosci.* **6**, 121 (2012).
50. Harris, K.M., Mahone, E.M. & Singer, H.S. Nonautistic motor stereotypies: clinical features and longitudinal follow-up. *Pediatr. Neurol.* **38**, 267–272 (2008).

ONLINE METHODS

Mice. All experimental manipulations on mice were performed in accordance with protocols approved by the Harvard Standing Committee on Animal Care and guidelines described in the US National Institutes of Health *Guide for the Care and Use of Laboratory Animals*. For electrophysiology studies, *Rbp4*-Cre transgenic mice (GENSAT #RP24-285K21) were bred to conditional channelrhodopsin-2 (ChR2) expressing mice expressing ChR2(H134R)-EYFP under control of an upstream *loxP*-flanked STOP cassette (Ai32; referred to as *ChR2$^{f/f}$*; The Jackson Laboratory #012569). For conditional deletion of the vesicular GABA transporter in cortical cells we used *Slc32a1*$^{f/f}$ mice (The Jackson Laboratory #012897). *Shank3B*$^{-/-}$ knockout mutant mice were described previously[23] and obtained from The Jackson Laboratory (#017688). All experiments using *Shank3B*$^{-/-}$ mice were performed in age matched littermates from breeding pairs between *Shank3B*$^{+/-}$ hererozygous animals. For optogenetic studies triple transgenic *Shank3*$^{+/-}$*; Rbp4-Cre; ChR2$^{f/wt}$* animals were cross bred in order to obtain *Cre* and *ChR2* expression in both heterozygous and Shank3B null backgrounds. In all experiments, male and female mice were used.

Viruses and stereotaxic intracranial injections. For intracranial injections, P0–7 mice were anesthetized with cold or isofluorane and placed into a stereotaxic apparatus. Viruses were delivered by injecting 100–200 nl at a maximum rate of 100 nl min^{-1} using a UMP3 microsyringe pump (WPI). For dendritic spine analysis of SPNs, AAVs expressing EGFP under the ubiquitous CAG promoter (AAV8-CAG-EGFP, Penn vector core) were injected in dorsomedial striatum using coordinates: 1 mm anterior to midpoint between ear and eye, 1 mm lateral from midline and 2.5 mm ventral to brain surface. For deletion of vGAT in cortical neurons, virus expressing Cre-EGFP under the neuron specific synapse promoter (AAV9-Syn-Cre-EGFP, Penn vector core) were injected in using coordinates: +1 mm and +2 mm anterior to midpoint between ear and eye, 1 mm lateral from midline, 0.5 mm ventral to brain surface. For chemogenetic reduction of cortical activity, P1–2 *Shank3B*$^{-/-}$*; Rbp4-Cre* mouse pups were injected bilaterally with AAV8-DI-hM4D$_i$-mCherry using the following coordinates: hM4Following injections and wound closure, mice received ketoprofen for analgesia and were returned to home cages for 8+ d.

Brain tissue processing and imaging. Mice were deeply anesthetized with isoflurane and perfused transcardially with 4% paraformaldehyde in 0.1 M sodium phosphate buffer. Brains were fixed for 24 h at 4 °C, washed in phosphate buffer saline (PBS) and sectioned (50 µm) coronally using a vibratome (Leica VT1000s). Brain sections were mounted on glass slides, dried and mounted with ProLong antifade reagent containing DAPI (Molecular Probes). Whole brain sections were imaged with an Olympus VS110 slide-scanning microscope. For dendritic spine analysis, high-resolution images of regions of interest were subsequently acquired using an Olympus FV1000 confocal microscope (Harvard Neurobiology Imaging Facility). Confocal stacks were acquired with a 63× objective and 0.75-µm spacing in Z. Confocal images were processed and analyzed using ImageJ software.

Acute slice preparation and electrophysiology. Acute brain slices and whole-cell recordings from SPNs were performed using standard methods, as described previously[6]. Briefly, mice (6–60 d old) were anesthetized by isoflurane inhalation and perfused transcardially with ice-cold artificial cerebrospinal fluid (ACSF) containing (in mM): 125 NaCl, 2.5 KCl, 25 $NaHCO_3$, 2 $CaCl_2$, 1 $MgCl_2$, 1.25 NaH_2PO_4 and 25 glucose (310 mOsm per kg). Cerebral hemispheres were removed, placed in cold choline-based cutting solution consisting of (in mM): 110 choline chloride, 25 $NaHCO_3$, 2.5 KCl, 7 $MgCl_2$, 0.5 $CaCl_2$, 1.25 NaH_2PO_4, 25 glucose, 11.6 ascorbic acid, and 3.1 pyruvic acid), and transferred into a slicing chamber containing ice-cold choline-based solution. Coronal slices including striatum (275 µm thick) were cut with a Leica VT1000s vibratome, transferred for 10 min to a holding chamber containing ACSF at 34 °C and subsequently maintained at 20–22 °C. All recordings were obtained within 5 h of slicing. Both cutting solution and ACSF were constantly bubbled with 95% O_2/5% CO_2. Individual slices were transferred to a recording chamber mounted on an upright microscope (Olympus BX51WI) and continuously perfused (1–2 ml per minute) with ACSF at 20–22 °C. Cells were visualized using a 40× water-immersion objective with infrared DIC optics. Whole-cell voltage- and current-clamp recordings were made from SPNs in dorsomedial regions of striatum. Patch pipettes (2–4 MΩ) pulled from borosilicate glass (BF150-86-7.5, Sutter Instruments) were filled either with a Cs^+-based internal solution containing (in mM) 130 $CsMeSO_4$, 10 HEPES, 1.8 $MgCl_2$, 4 Na_2ATP, 0.3 NaGTP, and 8 sodium phosphocreatine, 10 $CsCl_2$, 3.3 QX-314 (Cl^- salt), (pH 7.3 adjusted with CsOH; 295 mOsm per kg) for voltage-clamp recordings, or with a K^+-based low Cl^- internal solution composed of (in mM) 130 $KMeSO_3$, 3 KCl, 10 HEPES, 1 EGTA, 4 Mg-ATP, 0.3 Na-GTP, 8 sodium phosphocreatine (pH 7.3 adjusted with KOH; 295 mOsm) for current-clamp recordings. For all voltage-clamp experiments, errors resulting from voltage drop across the series resistance (<20 MΩ) were left uncompensated. For current-clamp recordings all voltages reported are corrected for a junction potential of ~8 mV. In all experiments GABAR currents were blocked with 20µM SR95531 hydrobromide (Tocris) to eliminate inhibition from local interneuron or collateral SPNs. For light-evoked AMPAR EPSC recordings ACSF contained 10 µM (R)-CPP and recordings were performed at −70 mV holding potential except for ages >P15 in which -20 mV holding potential was used to maximize voltage control. For mEPSC recordings, ACSF contained 1 µM TTX besides CPP and TTX. For current clamp recordings membrane potentials were corrected for a ~8-mV liquid junction potential. Voltage clamp recordings were performed at 20–22 °C and current clamp recordings at 32 °C. To activate ChR2-expressing fibers, light from a 473-nm laser (Opto engine LLC) was focused on the back aperture of the microscope objective to produce wide-field illumination of the recorded cell. TTL triggered pulses of light (5-ms duration; 6 mW mm^{-2} under the objective) were delivered at the recording site at 30-s intervals.

***In vivo* recordings and optogenetic stimulation in mouse pups.** Mouse pups (P10–16) were anesthetized with isoflurane and placed in a stereotaxic apparatus. After surgical removal of scalp and cleaning of the skull with saline and 70% ethanol, two craniotomies were made with a 0.25-mm burr micro drill at (AP- 0 mm; ML-2.0 mm and AP-0.3 mm; ML- +1.5 mm; from bregma) and sealed with Kwik-Cast silicone Elastomere. Animals were fitted with a custom-made titanium head bar using transparent glue (Loctite 454) and allowed to recover from anesthesia for 1 h on a heat pad at 38 °C. Following recovery from anesthesia, animals were head fixed and *in vivo* electrophysiological recordings were performed using 32 channel probes (A1x32-Poly2, 177 µm^2 site area, NeuroNexus Technologies) with recording sites spanning 750 µm. Cortical recordings were done by positioning the electrode tip 1,250 µm deep from the brain surface, whereas striatal recordings were performed at a 2,750-µm depth. Sessions of 20 min were recorded after a 10 min stabilization period, with ChR2 stimulation initiated at t = 10 min. Extracranial optogenetic stimulation was achieved by coupling a 200-µm core optical fiber placed 7–8 mm from the craniotomy site at a 45° angle to a 473-nm laser (Ciel, Laser Quantum). Light pulses were controlled with an Acousto-Optic Modulator (AA opto-Electronic) for fast shuttering and intensity control. Final light power was 45–50 mW and pulse width was 5 ms. All recordings were validated by post hoc serial histological analysis of electrode placement. For *in vivo* unilateral optogenetic stimulation a bare surface mount emitter blue LED (470 nm) with flattened epoxy lens was attached directly to the surface of the skull using transparent glue following a similar surgical procedure. In these experiments brain slices were prepared immediately after completion of the stimulation protocol.

Data acquisition and analysis. For whole-cell recordings, membrane currents and potentials were amplified and low-pass filtered at 3 kHz using Multiclamp 700B amplifier (Molecular Devices), digitized at 10 kHz and acquired using National Instruments acquisition boards and a custom version of ScanImage written in MATLAB (Mathworks). Off-line analysis was performed using custom routines written in MATLAB and Igor Pro (Wavemetrics). Statistical analyses were done using GraphPad PRIZM 5 software (GraphPad). For *in vivo* multi-unit recordings, data was filtered at 1-8000 Hz during acquisition, digitized at 40 kHz and sorted into single unit activity via principal component analysis using Plexon's Omniplex and Offline Sorter systems, respectively. Data were further analyzed using custom routines in IGOR Pro and Neuroexplorer v5. Burst analysis was performed using an unbiased statistical method based on inter stimulus interval (ISI) "surprise" factor that takes into account the differential Gaussian distribution of intra-burst AP ISIs compared to ISIs of all APs in the recorded train[51]. AP clusters were considered bursts if the number of APs was

doi:10.1038/nn.4260

>4 and surprise factor >5. All multi-unit activity data are represented as median ± interquartile range or mean ± s.e.m. and statistical tests used for each data set are specified in the main text. For two-group comparisons, statistical significance was determined by two-tailed Student's *t*-tests (parametric) or Mann-Whitney *U* tests (non-parametric). Multi-groups were analyzed using one-way ANOVA with Tukey correction (parametric) or Kruskal-Wallis with Dunn's multi comparison correction (non-parametric). *P* values less than 0.05 were considered statistically significant.

A **Supplementary Methods Checklist** is available.

51. Legéndy, C.R. & Salcman, M. Bursts and recurrences of bursts in the spike trains of spontaneously active striate cortex neurons. *J. Neurophysiol.* **53**, 926–939 (1985).